ARTICLES
PUBLISHED ONLINE: 23 MAY 2016 | DOI: 10.1038/NPHOTON.2016.94
nature photonics

Stain-free histopathology by programmable supercontinuum pulses

Haohua Tu[1*†], Yuan Liu[1,2†], Dmitry Turchinovich[3], Marina Marjanovic[1,2], Jens K. Lyngsø[4], Jesper Lægsgaard[5], Eric J. Chaney[1], Youbo Zhao[1], Sixian You[1,2], William L. Wilson[6], Bingwei Xu[7], Marcos Dantus[8] and Stephen A. Boppart[1,2,9,10*]

The preparation, staining, visualization and interpretation of histological images of tissue is well accepted as the gold standard process for the diagnosis of disease. These methods have a long history of development, and are used ubiquitously in pathology, despite being highly time- and labour-intensive. Here, we introduce a unique optical imaging platform and methodology for label-free multimodal multiphoton microscopy that uses a novel photonic-crystal fibre source to generate tailored chemical contrast based on programmable supercontinuum pulses. We demonstrate the collection of optical signatures of the tumour microenvironment, including evidence of mesoscopic biological organization, tumour cell migration and (lymph-) angiogenesis collected directly from fresh *ex vivo* mammary tissue. Acquisition of these optical signatures and other cellular or extracellular features, which are largely absent from histologically processed and stained tissue, combined with an adaptable platform for optical alignment-free programmable-contrast imaging, offers the potential to translate stain-free molecular histopathology into routine clinical use.

Histopathology, whether visualizing microstructures in standard haematoxylin and eosin (H&E) stained tissue sections or selectively labelling molecules with special immunohistochemical stains, has a long history of development and has been instrumental in biological and clinical laboratories for basic research as well as in hospital pathology laboratories for disease diagnosis (Supplementary Discussion 1). However, current histopathology techniques have several limitations. First, the histological–histochemical treatment of the tissue, including fixation, embedding, sectioning and staining, is well known to induce distortion artefacts and the loss of some biological components, thus dictating the subjectivity of subsequent image-based histopathological observations and interpretations. Second, typical histological processing, such as formalin-fixed paraffin-embedded (FFPE), H&E-stained histology, requires a significant amount of time, from ~10 h to a few days (less in the case of the frozen-section analysis specifically used in cancer surgery) and thus delays diagnosis, heightens patient stress, and presents a significant economic burden to society[1]. Third, cost ineffectiveness has been intrinsically associated with the more than 4,500 labour-intensive histological–histochemical processes and procedures developed predominantly between 1841 and 1950 (95%)[2].

Because of the time and labour required to process, prepare, stain and microscopically visualize the tissue, as well as the inherent destructive nature of standard histopathology, great efforts have been made to use multiphoton microscopy[3] for the molecular and cellular examination of unlabelled (fresh) pathological tissue or other biological specimens (Supplementary Table 1). Stain-free histopathology of fresh tissue within minutes has been achieved by diverse nonlinear optical processes[4–8], improving on conventional histotechnology based on single-photon microscopy, so that the time-consuming paradigmatic elements of standard histology procedures may be avoided. However, pathologists with no laser training find the ultrafast lasers of multiphoton microscopy difficult to use. In this study, we introduce a user-friendly optical source and platform capable of generating histochemically specific images, without the laser realignments normally required for multiphoton microscopy, and provide visualization of microstructures not routinely possible with current histological techniques. In contrast to many earlier studies that only demonstrated the diagnostic capability of multiphoton microscopy to approach that of H&E histology, we show that this versatile multimodal multiphoton microscopy platform based on a widely coherent supercontinuum source can visualize the biological organization of mesoscopic (micrometre-scale) constituents, discriminate cell types in connective tissue, quantify cellular metabolism and recognize well-known cancer indictors such as collective tumour cell invasion, tumour-associated collagen reorganization, angiogenesis and lymphangiogenesis *in situ* in freshly excised unstained (thick) tissues.

Our technology was first used for the observation of the spatial distribution of biological vesicles and elastin fibres in these fresh tissues. To accomplish this, we developed a multiphoton microscope (Supplementary Fig. 1) that employs a novel photonic-crystal fibre source and programmed electronic variables (rather than discrete optical alignment settings) to collect co-localized label-free images based on the endogenous contrast from two-photon auto-fluorescence (2PAF), three-photon auto-fluorescence (3PAF), second-harmonic generation (SHG), third-harmonic generation (THG) and coherent

[1]Beckman Institute for Advanced Science and Technology, University of Illinois at Urbana-Champaign, Urbana, Illinois 61801, USA. [2]Department of Bioengineering, University of Illinois at Urbana-Champaign, Urbana, Illinois 61801, USA. [3]Max Planck Institute for Polymer Research, Ackermannweg 10, Mainz 55128, Germany. [4]NKT Photonics A/S, Blokken 84, 3460 Birkerød, Denmark. [5]DTU Fotonik, Technical University of Denmark, Ørsteds Plads 343, 2800 Lyngby, Denmark. [6]Department of Materials Science and Engineering, Frederick Seitz Materials Research Laboratory, University of Illinois at Urbana-Champaign, Urbana, Illinois 61801, USA. [7]Biophotonic Solutions Inc., East Lansing, Michigan 48823, USA. [8]Department of Chemistry and Department of Physics, Michigan State University, East Lansing, Michigan 48824, USA. [9]Department of Electrical and Computer Engineering, University of Illinois at Urbana-Champaign, Urbana, Illinois 61801, USA. [10]College of Medicine, University of Illinois at Urbana-Champaign, Urbana, Illinois 61801, USA. †These authors contributed equally to this work. *e-mail: boppart@illinois.edu; htu@illinois.edu

© 2016 Macmillan Publishers Limited. All rights reserved

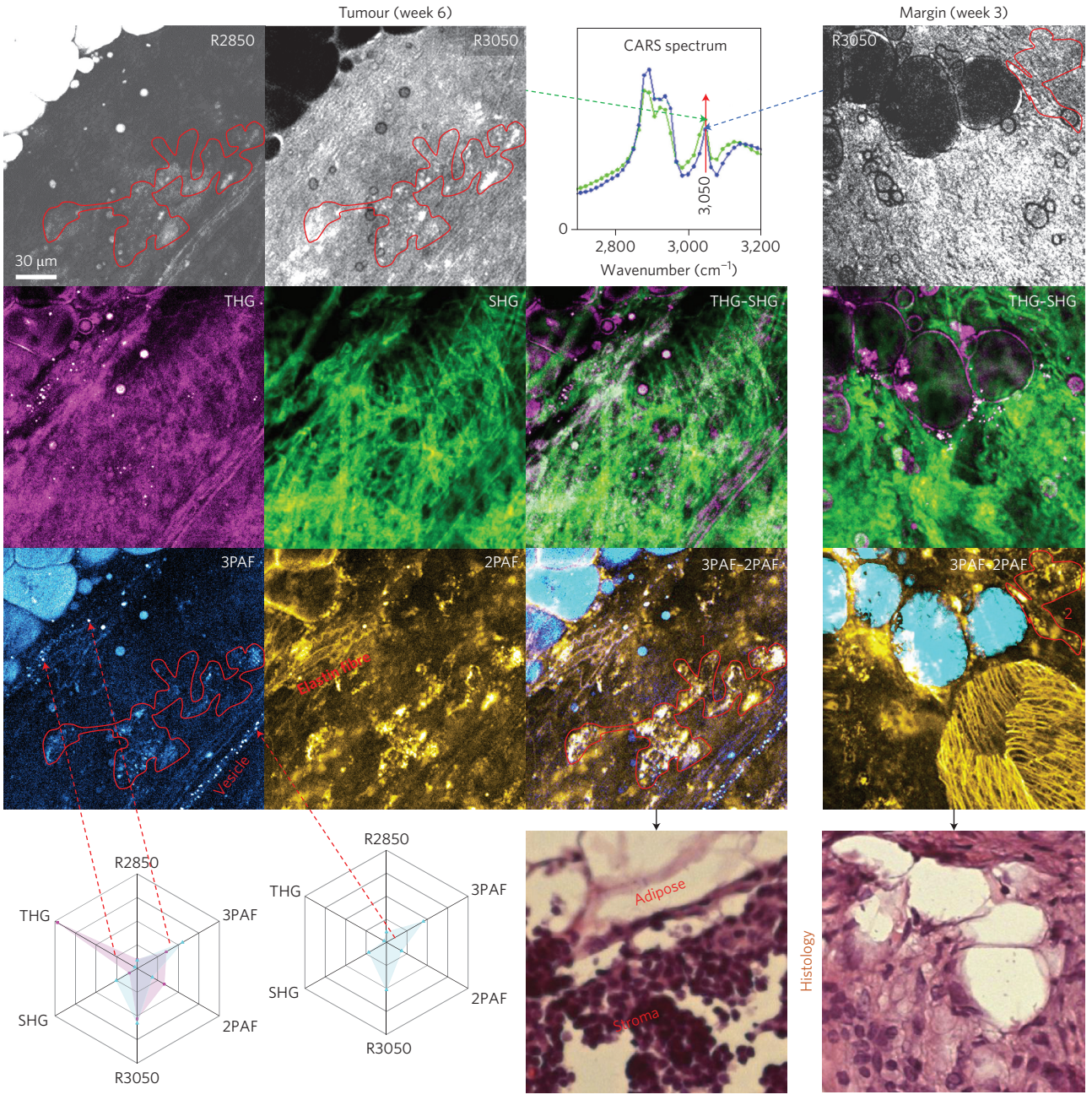

Figure 1 | Mesoscopic organization of biological microstructures revealed in co-localized multiphoton images of two rat mammary specimens and absent in corresponding FFPE–H&E histology images. Area-integrated CARS spectra over 34 hyperspectral images confirm the presence of a significant R3050 peak (see text for details) as a potential cancer biomarker. Left columns: Different histochemical components of a tumour are selectively revealed by different single-modality images. Cell cluster 1 (red outline) is identifiable in a 2PAF image and also in 3PAF, R3050 and R2850 images, indicating tumour-associated metabolism (see text for details). The hexagonal radar multiphoton profile (nine-pixel average) of a specific type of isolated vesicle approximates that of vesicles aligned in a tubular formation, suggesting that these vesicles are distributed more diffusely before organizing into a tube (indicative of angiogenesis, see text for details). Right column: Cell cluster 2 (red outline) in a specimen with histologically unidentified cancer from a carcinogen-injected rat is identifiable in a 2PAF image, but not in R3050 and other images, indicating normal cellular metabolism. Elastin fibres widely observed in connective tissue are shown to be organized into a 'basket', which can be linked to lymphangiogenesis (see text for details). Multiphoton image size: 380 × 380 pixels with 0.5 μm pixel size.

anti-Stokes Raman scattering (CARS) or stimulated Raman scattering (SRS) (Supplementary Tables 1 and 2)[9]. A well-known preclinical carcinogen-induced rat mammary tumour model[10] was used and a mammary tumour/tissue specimen (5 × 5 mm^2 area, ~1 mm thickness) was excised from a rat six weeks after carcinogen injection. Collection of the multimodal multiphoton images began within minutes after dissection from a site with cleanly delineated adipose and stromal regions, and standard H&E histology was subsequently performed to locate an anatomically similar site for comparison[6] (Fig. 1, left panel). Multiphoton images of R2850 versus R3050 (CARS response at 2,850 cm^{-1} versus 3,050 cm^{-1}; Fig. 1, top row), THG versus SHG (Fig. 1, second row) and 3PAF versus 2PAF (Fig. 1, third row) demonstrate the largely orthogonal signal contrast of lipids versus proteins/water[6,11], optical heterogeneity versus noncentrosymmetry, and blue autofluorescence versus yellow FAD autofluorescence[12], respectively. These multiple

© 2016 Macmillan Publishers Limited. All rights reserved

contrast mechanisms highlight the diverse histochemical and structural components of the specimen, particularly the 3PAF-visible micrometre-sized biological vesicles that appear spatially arranged in a tubular formation. The same field of view also displays some uniquely 2PAF-visible thin (~1 μm diameter) elastin fibres (EF) known to be present in mammary stroma (Supplementary Fig. 2). In a second specimen from the same animal, elastin fibres are shown to have organized into a 'basket' in adipocyte-infiltrated stroma (Fig. 1, right column).

The visualization of these structures is somewhat analogous to the visualization of hand bones in 1895 by X-ray radiography. Under ambient visible illumination, the bones are not visible due to the low detection sensitivity and high interfering background, even though the information is present. They emerge when the visible illumination is switched to X-ray irradiation at a different wavelength. Thus, imaging contrast from a fresh unstained tissue specimen can be generated by simply manipulating an irradiating wave that interacts with the specimen, rather than by manipulating (for example, histologically processing and staining) the specimen and irradiating it with a fixed wave. This methodology of clinical imaging[13] has largely been integrated into a number of radiological modalities (for example, ultrasound, CT, MRI and PET) and in multiphoton imaging, enabling stain-free histopathology[4–8] and allowing the imaging to rely more on physics (for example, wave propagation, electrical engineering and programming) than chemistry (wet laboratories, reagents, consumables and so on). Noticeably, the above visualization of these biological structures marks a shift from subcellular chemical contrast generation based on histological and histochemical sample treatments to one of light manipulation by programmable multiphoton irradiation and signal detection. The only changes in settings from one single-modality image in Fig. 1 to another are achieved by controlling the electronic amplitude–phase mask of the pulse shaper for tailored excitation to pair with a switchable spectral channel for signal detection (Supplementary Table 2) and an electronic setting of optical delay that sets the CARS vibrational frequency. Because these settings can be tuned rapidly (<10 ms) or switched under programmable control, different histochemical components can be selectively revealed in different single-modality images, highlighting our perception of 'seeing things in a different light'. By varying the light with agile pseudo-continuous programming, the contrast of these components against their background can be rapidly tuned to discover the otherwise obscured biological vesicles and fibres.

This imaging transformation and potential clinical translation of multiphoton microscopy is enabled by an emergent concept of laser-microscope alignment decoupling (Supplementary Fig. 1 and Supplementary Discussion 2), which requires a synergistic combination of deterministic single-mode coherent supercontinuum generation (Supplementary Discussion 3) and the arbitrary pulse shaping used typically in precision metrology or telecommunication applications[14] (Supplementary Discussion 4). Thus, an operator with no laser and optical alignment training could selectively display the spatial distribution of a specific endogenous substance on the computer screen, or instantly (and remotely if necessary) change the imaged substance to a different one by pushing preprogramed buttons that control the excitation/detection (Supplementary Table 1), with neither histological stains nor optical realignments.

In contrast to the vital signatures of various normal adipocytes, mast cells and fibroblasts that are uniquely reflected by cell bodies (Fig. 2), tumour cells are shown in 2PAF–SHG composite images to emerge from the metastatic environment of the crosslinked collagen network[15] inside a week 3 tumour, and are shown to be invading the surrounding stroma in a week 8 tumour consisting of tumour-associated collagen signatures-2 (TACS-2) fibres that are aligned parallel to the tumour boundary[16,17] (Fig. 2). These normal and tumour-associated signatures are absent in comparable H&E histology images of the same specimens due to the low or non-specific contrast of the extracellular matrix. The multiphoton images not only convey the unperturbed morphological information from various cells and the extracellular matrix, but also discriminate between tumour and normal cells via the 3PAF/2PAF signal ratio. The adipocytes (cell indicated by '3' in Fig. 2), mast or other stromal cells (cells 4 and 5) and fibroblasts (cell 6) have a relatively small 3PAF signal, so they retain their yellow 2PAF colour in the 2PAF–3PAF composite images. In contrast, the tumour cells (for example, cell 7) in both tumours generate a large co-localized 3PAF signal (presumably due to high levels of NADH during tumour-associated metabolism[18]), which gives these cells a blue appearance. An invasion front at the tumour–stroma boundary can be identified in the week 8 tumour by the invading tumour cells and the numerous 'disorganized' 3PAF-lightened vesicles seemingly derived from the tumour cells. The presence of a significant co-localized 3PAF signal can then discriminate the tumour cells in the week 6 tumour (Fig. 1, cell cluster 1) from the normal cells in the week 3 tumour margin specimen (Fig. 1, cell cluster 2), despite their similar irregular morphology. Small but appreciable R2850 (lipid) signals can also be found to co-localize with the 2PAF-visible tumour cells (Fig. 1, left, R2850 image) but not the normal cells in Fig. 2, suggesting *de novo* lipogenesis associated with the tumour cells[19,20]. Experienced pathologists can discriminate tumour and non-tumour cells/specimens from the histology images alone (Figs 1 and 2), but cannot necessarily deduce any metabolic information.

We were also able to demonstrate a potential quantitative breast cancer biomarker in this rat model. The tumours can be objectively discriminated against non-tumour specimens by the emergence of an R3050 spectral peak in the hyperspectral image-integrated CARS spectra (Figs 1 and 2). This R3050 signal is not from the carcinogen (*N*-nitroso-*N*-methylurea) injected into the rats, because spectral focusing of CARS on a saturated water solution of the carcinogen (1.4% by weight) did not yield any signal at R3050. Because regions within mammary specimens can be largely classified into stromal regions (Supplementary Fig. 2) and adipose regions (Supplementary Fig. 3) that account for 25 and 75% of the total area from control specimens, respectively, it is more representative to examine comparable tumour and non-tumour specimens that contain both regions (Supplementary Fig. 4). The R3050 spectral peak readily differentiates tumour and non-tumour specimens, even though their morphological differences are subtle and tumour cells may not be present. By comparing Supplementary Fig. 4 with the multimodal images and the integrated CARS spectra from the stromal regions (Supplementary Fig. 2) and adipose regions (Supplementary Fig. 3), we can conclude that this peak emerges only from the stromal regions. In videos consisting of hyperspectral CARS images, the cancer biomarker manifests itself as a 'flash' at R3050 in the stromal regions but not in the adipose regions (Supplementary Movies 1–3). This potential biomarker is robust against the presence of various marked structures that could have complicated qualitative morphological-based interpretation (Figs 1 and 2 and Supplementary Fig. 2). Because this region-dependent hyperspectral cancer biomarker cannot be appreciated by either imaging or spectroscopy alone, the advantage of hyperspectral CARS imaging for the detection and spatial mapping of this biomarker is self-evident.

In all tumour specimens (Figs 1 and 2 and Supplementary Figs 2 and 4), considerable R3050 signal was co-localized with the 2PAF-visible tumour cells, and was more pronounced than the R2850 signal that reflects *de novo* lipogenesis and thus gives these cells a grey appearance in the composite 2PAF–R3050 images (Figs 1 and 2). Non-tumour cells have little contrast in both the R3050 and R2850 images (Figs 1 and 2 and Supplementary Figs 2 and 4). Also, mammary tumours seem to generate the R3050-peak

© 2016 Macmillan Publishers Limited. All rights reserved

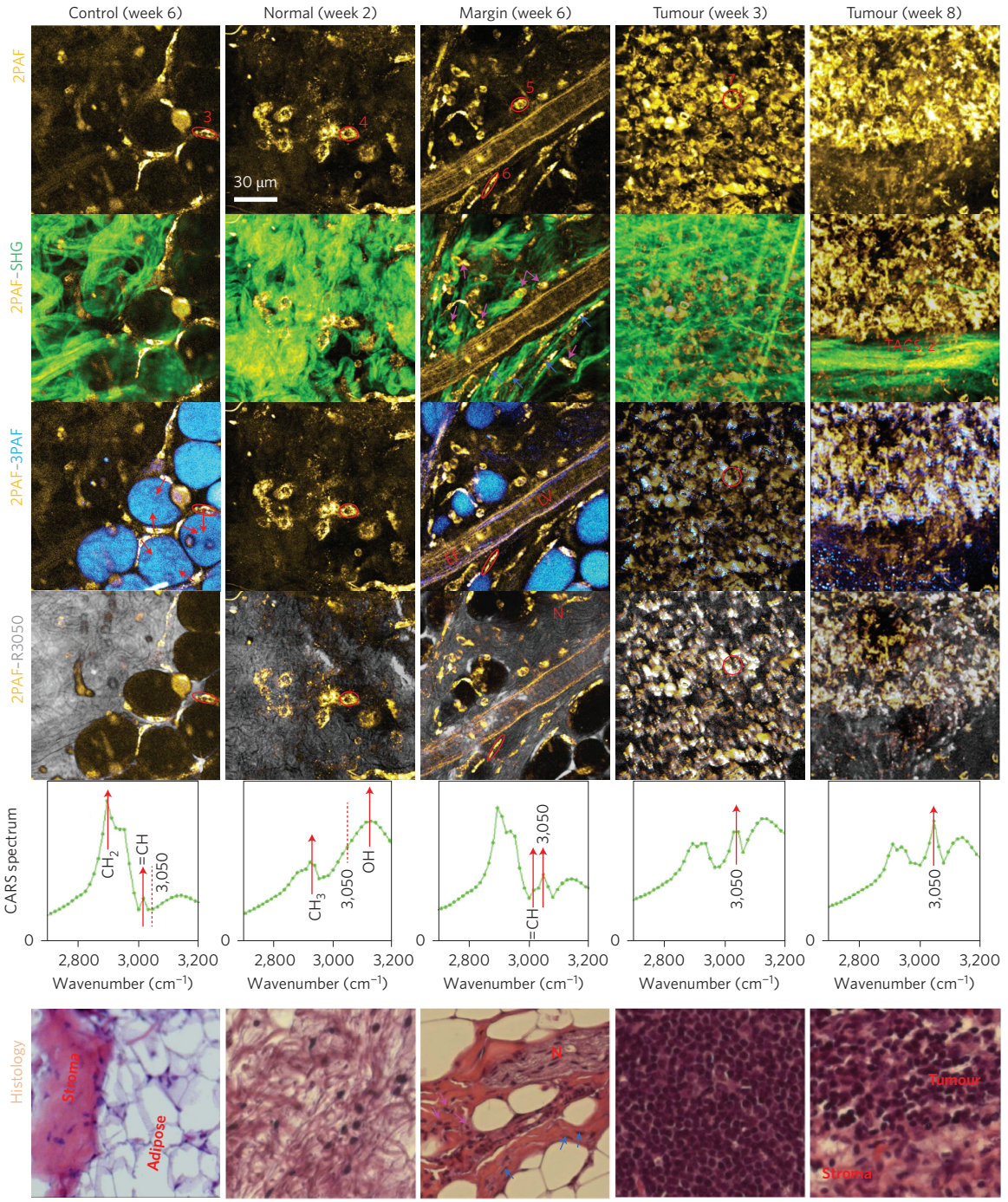

Figure 2 | Optical signatures in co-localized multiphoton images of five mammary specimens that are absent in corresponding FFPE–H&E histology images. Area-integrated CARS spectra over 30 hyperspectral images reveal common molecular vibrations of CH_2 (2,850 cm^{-1}), CH_3 (2,930 cm^{-1}), =CH (3,015 cm^{-1}) and OH stretches (3,000–3,200 cm^{-1}), and exhibit a cancer biomarker at R3050, whereas cross-modality visibilities of 2PAF-enhanced cells (encircled in red and labelled 3 to 7) represent distinct cellular metabolic states. Red arrows and red dashed lines are used to label observable and unobservable peaks, respectively. Bottom row: Histology delineates characteristic adipose and stromal regions of control mammary tissue and reveals cell nuclei located in interstitial spaces among lipid vacuoles of adipocytes with no correspondence between cell nuclei and lipids. In multiphoton images, however, 2PAF-visible cell bodies in the background of 3PAF-visible lipids point to the unique relationship between the cell bodies and lipids (red arrows) that form complete adipocytes. Bottom row, second left: Histology of a stroma-only region from a normal appearing mammary specimen (no palpable tumour) from a carcinogen-injected rat displays only some cell nuclei scattered in a distorted collagen fibre network, whereas multiphoton images show how several cells orient themselves in the voids of the collagen fibre network. Bottom row, middle: Histology identifies fibroblasts (blue arrows) from mast cells (magenta arrows) at a tumour margin ~1 mm away from a palpable week 6 tumour. In multiphoton images, however, spindle-shaped collagen-producing fibroblasts are aligned with SHG-visible collagen fibres and can be easily differentiated from mast cells near a lymphatic vessel (LV) with flowing lymph (Supplementary Movie 4) and a leaky 2PAF-visible basement membrane containing elastin fibres. Second right: Multiphoton images of the inside of a non-palpable tumour reveal a crosslinked collagen network that assists tumour invasion. Right: Multiphoton images at a tumour–stroma boundary exhibit vital signatures of local tumour invasion across TACS-2 collagen. EF, elastin fibres; N, nerve; TACS, tumour-associated collagen structure. Multiphoton image size: 380 × 380 pixels with 0.5 μm pixel size.

© 2016 Macmillan Publishers Limited. All rights reserved

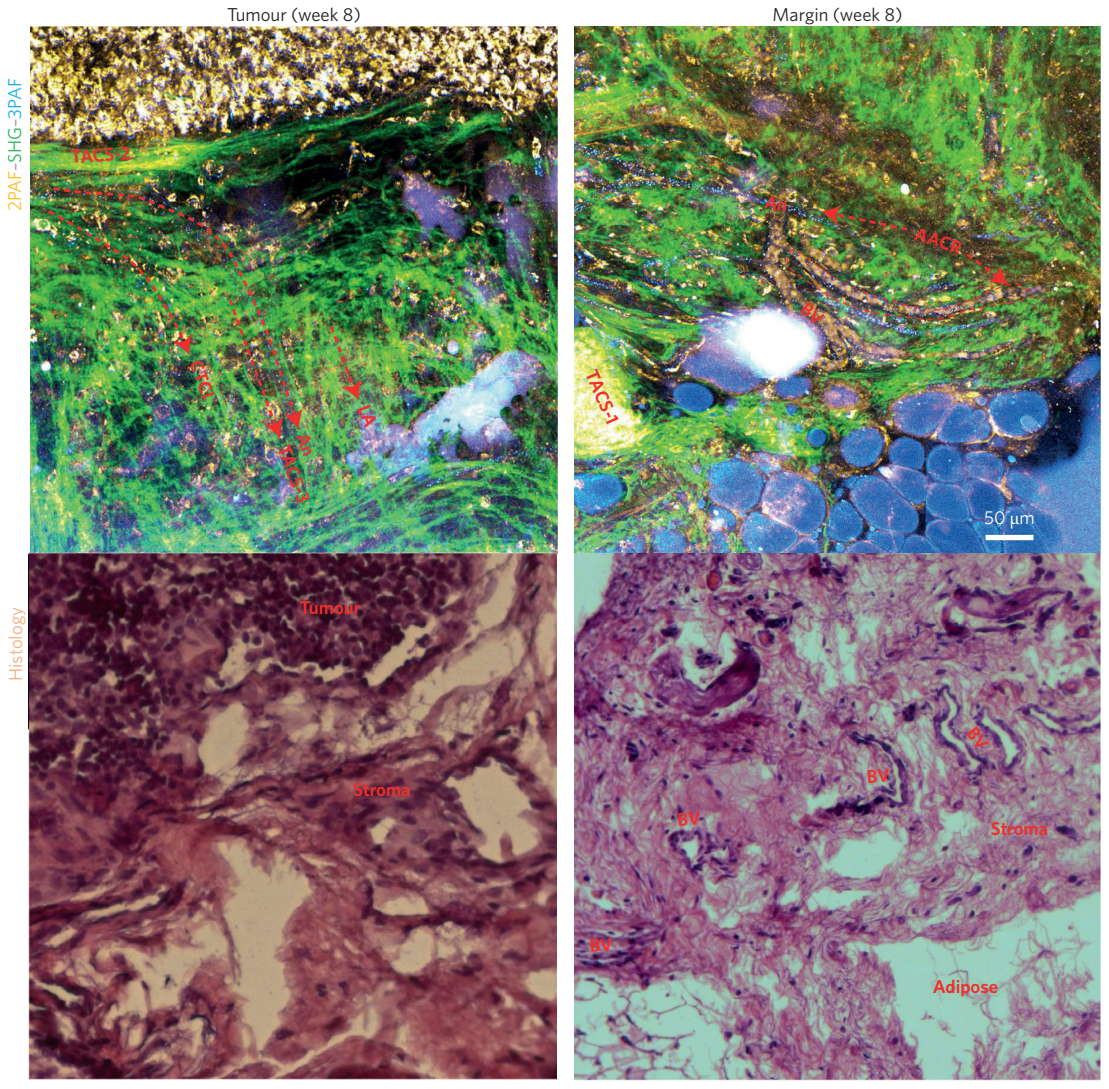

Figure 3 | Optical signatures of local tumour invasion in large-area tri-modal multiphoton images of two rat mammary specimens that are absent in corresponding FFPE–H&E histology images. The margin specimen was excised ~1 mm away from the tumour. Directed local tumour invasion (downward in image) at the tumour–stroma boundary (left) and degradation of adipose tissue by vascularized stroma at the tumour margin (right) are recognized in the multiphoton images, but only the former can be revealed in standard H&E histology. In the latter case, the 3PAF-visible angiogenesis (An) is absent, and naturally branched 2PAF-visible blood vessels (BV) become distorted and fragmented in the histology image so that the tumour-associated angiogenesis is hardly detectable. In both cases, several vital optical signatures (arrows) of local tumour invasion are largely obscured by a strong interfering background in the tri-modal multiphoton images, just like in histology, but emerge when the contrasts of individual multiphoton modalities are unmixed (Supplementary Figs 6–9; see text for details). AACR, angiogenesis-accommodating collagen reorganization; CTCI, collective tumour cell invasion; LA, lymphangiogenesis; TACS, tumour-associated collagen structure. Multiphoton image size: 1,100 × 1,100 pixels with 0.5 μm pixel size.

phenotype, which was also widely found in normal spleen, liver, lung, skin and muscle from control rats. The mammary tumour cells in Fig. 2 resemble the biosynthesis-active normal cells in the spleen and liver, which exhibit co-localized cell contrast from 2PAF, R3050 and R2850 (Supplementary Fig. 5). This evidence suggests that the metabolic biomolecules associated with the on-and-off R3050 breast cancer biomarker are produced by the tumour cells with a metabolism switched to mainly biosynthesis (Warburg effect)[21] and become transported away from the tumours to the tumour margins (Fig. 1, right; Fig. 2, middle). These findings suggest that the histologically normal specimens exhibit evidence of this R3050 biomarker and its association with early changes in carcinogenesis. These results suggest that the R3050 cancer biomarker could potentially enable cancer diagnosis at a very early stage (week 1), when no tumour is palpable and gross examination is indeterminate (Supplementary Table 3). The observation of a similar cancer biomarker in humans would potentially allow for early and quantitative diagnosis from small biopsy specimens that may or may not sample the tumours directly.

As a second example, multiphoton images of a week 8 tumour in Fig. 2 demonstrate the migration of 2PAF/R3050-visible tumour cells or cell debris that collectively represent tumour cell migration/invasion[22] (collective tumour cell invasion, CTCI, Fig. 3, left panel; Supplementary Fig. 6). The 'disorganized' 3PAF-visible vesicles in Fig. 2 become part of another extension of organizing vesicles infiltrating from the tumour into the surrounding stroma (An, Fig. 3, left panel; Supplementary Figs 6–8). In another specimen, there is image-based evidence that the vascularized stroma in the cancerous tissue is degrading adipose tissue, supporting findings from the previous literature that these vesicles can be linked to angiogenesis[23,24], a known hallmark of cancer[25]. The relatively well developed blood vessels (BV) have 2PAF-visible internal epithelial cells but sparse 3PAF-visible vesicles, while the angiogenic vessels (An) have no such epithelial cells but show an abundance of such vesicles

© 2016 Macmillan Publishers Limited. All rights reserved

(Fig. 3, right). Similar to the adipocytes, mast cells and fibroblasts in Fig. 2, these vasculature-revealing epithelial cells have minimum (or uniform) contrast in 3PAF (or CARS) (Supplementary Figs 8 and 9) and are therefore suggestive of non-malignant normal cells. Unlike angiogenesis via the classic sprouting mechanism[26], the observed angiogenesis is accompanied by reorganized collagen networks (Supplementary Fig. 8), including a third extension of TACS-3 collagen fibres perpendicular to the TACS-2 collagen fibres[16,17] to assist CTCI (Fig. 3, left) and angiogenesis-accommodating collagen reorganization. A TACS-1 aggregate of fibrosis can also be identified[16,17] (Fig. 3, right). Numerous elastin fibres form a fourth extension in concert with the above three (LA, Supplementary Fig. 6) and may be associated with the formation of the elastin basket in Fig. 1, to ultimately evolve into the leaky elastin-containing basement membrane known to enclose lymphatic vessels (LV, Fig. 2; Supplementary Movie 4), that is, to enable tumour lymphangiogenesis[27] (LA, Supplementary Fig. 7).

These linked events of CTCI, tumour-associated collagen reorganization and (lymph-)angiogenesis reflect the vital signatures of local tumour invasion present in fresh tissue being imaged with this multimodal multiphoton microscope. Although experienced pathologists can identify the tumour cells and high-density distorted blood vessels suggestive of angiogenesis in comparable histology images (Fig. 3), the additional information and findings from the fresh tissue microenvironment of local tumour invasion are often missing due to the weak signal, strong interfering background and histology-induced structural changes (Figs 1 and 2). It should be noted that the four parallel extensions of tumour cells or cell debris, angiogenic vesicles, reorganized collagen fibres and lymph-angiogenic elastin fibres are largely obscured by the strong interfering background in the composite multimodal image (Fig. 3, left panel), but emerge when the imaging contrasts are unmixed (Supplementary Fig. 6). It is then conceivable that the absence of these optical signatures in the comparable histology images originates more from contrast interference than a lack of signal. Thus, the arbitrary mixing and unmixing of a large number (>5) of different contrasts (Figs 1–3 and Supplementary Figs 2–9) makes our stain-free histopathology advantageous over standard histopathology.

To conclude, the use of stain-free histopathology offers several significant advantages. Rapid, stain-free imaging of fresh thin or thick tissue specimens is possible with short turnaround times for disease diagnosis, and could even supersede surgical frozen-section analysis, in contrast to more conventional histological tissue fixation, processing and staining that often requires lengthy preparation time. Image generation can result from a microscope platform without the need for extensive wet laboratory facilities and a team of histotechnologists. Without the need for tissue fixation and processing, including the use of formalin[28], xylene[29] and other toxic chemicals, there are possible environmental and healthy workplace benefits. Although our stain-free histopathology will not completely replace standard H&E histopathology as the gold standard, the haematoxylin, eosin, other histochemical stains and antibody or nucleic acid immunohistochemistry probes may be replaced by the programmable light that generates tailored chemical contrasts, not only from the demonstrated five modalities but also from transient[5] or nonlinear absorption[30], stimulated emission[31], wave mixing[32] platforms, and so on. Because the light served as a programmable variable within a broad excitation/detection map that was tailored to probe specific endogenous substances (Supplementary Table 2), it can be easily reprogrammed to target different substances of interest, as well as biological samples with varying chemical composition and interfering backgrounds (Supplementary Table 1). The 'virtual' histochemistry achieved by manipulating light has advantages over current immunohistochemistry because a large number of molecular markers can be imaged in a single tissue section to maximize the information at each pixel and capture crucial co-relationships between the markers (Figs 1–3). Without the diverse molecular contrast from multiphoton interactions, this 'virtual' histochemistry has been difficult to achieve in single-photon technologies based on confocal reflectance microscopy[33] (reflectance contrast), optical coherence tomography[34] (scattering contrast) and photoacoustic imaging[35] (absorption contrast). As representative data, this study demonstrates several known as well as new potential cancer biomarkers based on multimodal morphological and spectral signatures. Future investigations will use these data to further elucidate the complex mechanisms and biochemical processes in carcinogenesis as well as in other pathological processes in pre-clinical and clinical specimens.

Methods

Methods and any associated references are available in the online version of the paper.

Received 1 July 2015; accepted 18 April 2016;
published online 23 May 2016

References

1. Titford, M. & Bowman, B. What may the future hold for histotechnologists? *Lab. Med.* **43,** e5–e10 (2012).
2. Buesa, R. J. Histology: a unique area of the medical laboratory. *Ann. Diagn. Pathol.* **11,** 137–141 (2007).
3. Denk, W., Strickler, J. H. & Webb, W. W. Two-photon laser scanning fluorescence microscopy. *Science* **248,** 73–76 (1990).
4. Zipfel, W. R. *et al.* Live tissue intrinsic emission microscopy using multiphoton-excited native fluorescence and second harmonic generation. *Proc. Natl Acad. Sci. USA* **100,** 7075–7080 (2003).
5. Matthews, T. E., Piletic, I. R., Selim, M. A., Simpson, M. J. & Warren, W. S. Pump–probe imaging differentiates melanoma from melanocytic nevi. *Sci. Transl. Med.* **3,** 71ra15 (2011).
6. Ji, M. *et al.* Rapid, label-free detection of brain tumors with stimulated Raman scattering microscopy. *Sci. Transl. Med.* **5,** 201ra119 (2013).
7. Tao, Y. K. *et al.* Assessment of breast pathologies using nonlinear microscopy. *Proc. Natl Acad. Sci. USA* **111,** 15304–15309 (2014).
8. Lu, F.-K. *et al.* Label-free DNA imaging *in vivo* with stimulated Raman scattering microscopy. *Proc. Natl Acad. Sci. USA* **112,** 11624–11629 (2015).
9. Zipfel, W. R., Williams, R. M. & Webb, W. W. Nonlinear magic: multiphoton microscopy in the biosciences. *Nature Biotechnol.* **21,** 1369–1377 (2003).
10. Sukumar, S., Notario, V., Martin-Zanca, D. & Barbacid, M. Induction of mammary carcinomas in rats by nitroso-methylurea involves malignant activation of H-ras-1 locus by single point mutations. *Nature* **306,** 658–661 (1983).
11. Chowdary, P. D. *et al.* Molecular histopathology by spectrally reconstructed nonlinear interferometric vibrational imaging. *Cancer Res.* **70,** 9562–9569 (2010).
12. Chance, B., Schoener, B., Oshino, R., Itshak, F. & Nakase, Y. Oxidation–reduction ratio studies of mitochondria in freeze-trapped samples. NADH and flavoprotein fluorescence signals. *J. Biol. Chem.* **254,** 4764–4771 (1979).
13. Sutton, D. *A Textbook of Radiology and Imaging* (Churchill Livingstone, 1987).
14. Weiner, A. M. Femtosecond pulse shaping using spatial light modulators. *Rev. Sci. Instrum.* **71,** 1929–1960 (2000).
15. Levental, K. R. *et al.* Matrix crosslinking forces tumor progression by enhancing integrin signaling. *Cell* **139,** 891–906 (2009).
16. Provenzano, P. P. *et al.* Collagen reorganization at the tumor–stromal interface facilitates local invasion. *BMC Med.* **4,** 38 (2006).
17. Provenzano, P. P. *et al.* Collagen density promotes mammary tumor initiation and progression. *BMC Med.* **6,** 11 (2008).
18. Skala, M. C. *et al. In vivo* multiphoton microscopy of NADH and FAD redox states, fluorescence lifetimes, and cellular morphology in precancerous epithelia. *Proc. Natl Acad. Sci. USA* **104,** 19494–19499 (2007).
19. Menendez, J. A. & Lupu, R. Fatty acid synthase and the lipogenic phenotype in cancer pathogenesis. *Nature Rev. Cancer* **7,** 763–777 (2007).
20. Le, T. T., Huff, T. B. & Cheng, J. X. Coherent anti-Stokes Raman scattering imaging of lipids in cancer metastasis. *BMC Cancer* **9,** 42 (2009).
21. Vander Heiden, M. G., Cantley, L. C. & Thompson, C. B. Understanding the Warburg effect: the metabolic requirements of cell proliferation. *Science* **324,** 1029–1033 (2009).
22. Friedl, P. & Gilmour, D. Collective cell migration in morphogenesis, regeneration and cancer. *Nature Rev. Mol. Cell Biol.* **10,** 445–457 (2009).
23. Carmeliet, P. & Jain, R. K. Angiogenesis in cancer and other diseases. *Nature* **407,** 249–257 (2000).
24. Weis, S. M. & Cheresh, D. A. Tumor angiogenesis: molecular pathways and therapeutic targets. *Nature Med.* **17,** 1359–1370 (2011).
25. Hanahan, D. & Weinberg, R. A. Hallmarks of cancer: the next generation. *Cell* **144,** 646–674 (2011).

© 2016 Macmillan Publishers Limited. All rights reserved

26. Folkman, J. & Haudenschild, C. Angiogenesis *in vitro*. *Nature* **288,** 551–556 (1980).
27. Stacker, S. A., Achen, M. G., Jussila, L., Baldwin, M. E. & Alitalo, K. Lymphangiogenesis and cancer metastasis. *Nature Rev. Cancer* **2,** 573–583 (2002).
28. Buesa, R. J. Histology without formalin? *Ann. Diagn. Pathol.* **12,** 387–396 (2008).
29. Buesa, R. J. Histology without xylene. *Ann. Diagn. Pathol.* **13,** 246–256 (2008).
30. Fu, D. *et al.* High-resolution *in vivo* imaging of blood vessels without labeling. *Opt. Lett.* **32,** 2641–2643 (2007).
31. Min, W. *et al.* Imaging chromophores with undetectable fluorescence by stimulated emission microscopy. *Nature* **461,** 1105–1109 (2009).
32. Mahou, P. *et al.* Multicolor two-photon tissue imaging by wavelength mixing. *Nature Methods* **9,** 815–818 (2012).
33. González, S. & Tannous, Z. Real-time, *in vivo* confocal reflectance microscopy of basal cell carcinoma. *J. Am. Acad. Dermatol.* **47,** 869–874 (2002).
34. Huang, D. *et al.* Optical coherence tomography. *Science* **254,** 1178–1181 (1991).
35. Zhang, H. F., Maslov, K., Stoica, G. & Wang, L. V. Functional photoacoustic microscopy for high-resolution and noninvasive *in vivo* imaging. *Nature Biotechnol.* **24,** 848–851 (2006).

Acknowledgements

This research was supported by grants from the National Institutes of Health (R01 CA166309 and R01 EB013723), the Danish Council for Independent Research – Technology and Production Sciences (FTP project ALFIE), the European Commission (EU Career Integration Grant 334324 LIGHTER) and by the Max Planck Society.

Author contributions

H.T., Y.L. and S.A.B. conceived the idea, performed the analysis and wrote the manuscript. H.T., Y.L. and Y.Z. built the microscope and conducted optical experiments. H.T., D.T. and J.L. tested and improved the long-term stability of the fibre supercontinuum source. J.K.L. fabricated a variety of photonic-crystal fibres for the supercontinuum source. W.L.W. characterized the supercontinuum source. E.J.C., S.Y. and M.M. performed biological experiments. B.X. and M.D. built the pulse shaper. H.T. and S.A.B. obtained funding for this research.

Additional information

Supplementary information is available in the online version of the paper. Reprints and permissions information is available online at www.nature.com/reprints. Correspondence and requests for materials should be addressed to H.T. and S.A.B.

Competing financial interests

M.D. is the founder of Biophotonic Solutions Inc., and has financial interest in a proprietary pulse shaping technology using multiphoton intrapulse interference phase scan (MIIPS).

© 2016 Macmillan Publishers Limited. All rights reserved

Methods

Fibre supercontinuum generation. Pulses (1,041 nm, 220 fs, 80 MHz) from a Yb:KYW laser (femtoTRAIN IC model-Z, High Q Laser) were coupled by an aspheric lens (C330TME-C, Thorlabs) into a 21 cm custom-made photonic-crystal fibre (NL-1050-NEG-PM-FUD, NKT Photonics) along the slow axis of the fibre[36]. The linear birefringence of the fibre was estimated to be 4.2×10^{-4} by spectral interferometry, ensuring small (<0.5%) nonlinear depolarization along the fast axis of the 21 cm fibre. Thus, the variation of the spectrum due to environmental changes was completely suppressed. The output (input) coupling power was maintained at 480 mW (800 mW) during all imaging sessions using a feedback control loop (Supplementary Fig. 1e). The output was collimated by an off-axis parabolic mirror and sent to the microscope. The parabolic mirror was aligned by optimizing the beam shape on a beam profiler at a long distance. The supercontinuum spectrum (780–1,320 nm) was measured using an optical spectral analyser daily to ensure reproducible operation. Throughout a one-year test period, this spectrum and the corresponding spectral phase were reproducibly measured in these daily operations, not only for one fibre segment but also for other 21 cm fibre segments, thus demonstrating the reliable spectral phase stability of this source and ensuring reproducible output power and polarization in routine daily operations. Without either the short-term quantum-noise instability or the long-term birefringence-induced instability[36], the supercontinuum enables high-quality multiphoton imaging of unstained biological samples.

Multimodality-empowered CARS microscope. A dichroic mirror (DMLP900, Thorlabs) was used to separate the supercontinuum into the CARS pump beam (780–880 nm) and the CARS Stokes beam (900–1,320 nm) (Supplementary Fig. 1e). The Stokes beam was sent into a commercial pulse shaper (MIIPS Box640, Biophotonics Solutions), not only for CARS imaging, but also for 2PAF, SHG, 3APF and THG imaging. The two beams were then recombined by another dichroic mirror, steered into a commercial microscope (BX61WI, Olympus) and focused by a super-apochromat objective (UPLSAPO ×60 W/IR NA = 1.20, Olympus). The super-apochromat microscope objective enabled diffraction-limited imaging, independent of the excitation wavelength. Because many common micrometre-sized biological vesicles show up in all imaging modalities of rat spleen and liver specimens, co-localized multimodal imaging at the same imaging plane could be ensured (Supplementary Fig. 5). All multiphoton signals were collected in the backward (epi-) direction by the same objective, spectrally filtered, detected by a common photomultiplier tube (H7421-40 Hamamatsu) and rigorously calibrated (Supplementary Methods), allowing *ex vivo* diagnosis of thick tissues (Supplementary Fig. 9). A specimen (typical area of 5×5 mm^2 and thickness of ~1 mm) was placed on a microscope slide and sealed under a coverslip, and the imaging focal plane was placed ~10 μm below the sample surface. A relatively long pixel dwell time of 200 μs was used for all modalities, which was largely limited by the raster scanning speed (>100 μs pixel dwell time) of the mechanical stage used to collect images. For the regular images (380×380 pixels, 0.5 μm pixel size) and large-area images ($1{,}100 \times 1{,}100$ pixels, 0.5 μm pixel size) presented in this study, 40 s and 5 min were required to collect each image, respectively.

All SHG, THG, CARS and 2PAF images were plotted with the same dynamic range using the default setting of ImageJ (National Institutes of Health) from unprocessed raw data. For some 3PAF images with low signals but recognizable morphological features, we tuned the dynamic range (brightness/contrast) to better show these features. Thus, our preprogrammed settings allowed a direct comparison of all modalities within the dynamic range, except for 3PAF. Although 3PAF does not generate strong signals in some specimens, it does in other specimens, and uniquely reveals a class of biological vesicles.

Pulse-shaping-enabled 'virtual' histochemistry. For 2PAF, SHG, 3APF and THG imaging of endogenous molecules and structures, pulses of selected spectral ranges were compressed to the transform limit by multiphoton intrapulse interference phase scanning[37] using the technique of 'local compression'[36]. The pulse shaper was used to spectrally select (and attenuate if necessary) the spectral bands (amplitude shaping) and to compensate the spectral phases measured at the objective focus (phase shaping)[38]. For CARS, an additional linear chirp of 4,500 fs^2 after pulse compression was introduced into the Stokes beam by phase shaping for the optimal performance of spectral focusing[39] within the detection vibrational band of 2,700–3,200 cm^{-1}. The spectrally focused vibrational frequency of CARS was controlled by electrically setting the optical delay between the pump and Stokes pulses (Supplementary Fig. 1). The spectral resolution of the system was calculated to be 14 cm^{-1} based on the measured full-width at half-maximum (19 cm^{-1}) of the 2,913 cm^{-1} peak in the CARS spectrum of dimethyl sulfoxide (Supplementary Methods). This finite spectral resolution of CARS is mostly limited by the finite spectral resolution of the pulse shaper (640 pixels to cover the 750–1,350 nm bandwidth). Spectral-focusing CARS was then used to collect hyperspectral CARS images from the biological samples, each of which was obtained at one spectral-focusing delay that was varied among the images. The CARS spectral intensity at each spectral-focusing delay (vibration frequency) was calculated by averaging the intensity of all pixels in the hyperspectral image corresponding to that vibration frequency. This simple treatment mimics wide-field Raman spectroscopy and was sufficient to distinguish tumour and normal specimens (Supplementary Fig. 4). Thus, pulse shaping enables optimization of optical signal generation across different modalities. The amplitude and compensation phase masks were then preprogrammed and applied in all imaging sessions. This can then demonstrate that exposing a biological sample to pulse-shaped excitations generates an imaging contrast similar to staining the sample with various dyes or fluorescent antibodies. In other words, the endogenous biomolecules in various biological samples can be 'artificially' (non-invasively) labelled by pulse-shaped excitations along certain detection spectral channels, rather than being 'physically' labelled by exogenous stains or other fluorescent agents.

Animal model and histology. Pre-clinical rat experiments were performed under a protocol approved by the Institutional Animal Care and Use Committee at the University of Illinois Urbana–Champaign. Female rats forming one group (F344, Harlan, seven weeks old) were injected intraperitoneally with *N*-nitroso-*N*-methylurea (Sigma) at a concentration of 55 mg kg^{-1} to induce mammary tumours[10]. The left abdominal side received one injection and the right abdominal side received a second injection of equal dose one week later. This pre-clinical rat model is well established and known to induce mammary tumours reproducibly and deterministically through single point mutations. This model is suitable for investigating breast cancer development because the anatomical and pathological features, the hormone dependency and the immunohistochemical responses of the lesions mimic human ductal carcinoma *in situ* (DCIS)[40–42]. Around 5 weeks after the second injection, tumours were palpable from the abdominal surface. An equal amount of saline was injected into the control rats to account for any possible effects from the physical injection. In a longitudinal study, nine experimental and nine control rats were euthanized 1–9 weeks after the second injection, and mammary tissue specimens and other organs were dissected and placed in saline before imaging (Supplementary Table 3).

During gross examination, excised mammary tissue was cut into small specimens (typically 5×5 mm^2 area, 1–2 mm thickness) for multiphoton imaging. Tumour margin specimens were excised at sites 1–5 mm away from palpable tumours (orange-coloured granular formation). Standard FFPE–H&E histology was performed on some specimens, and histology images corresponding to the multiphoton images were obtained by searching similar areas under a microscope. Although best efforts were made to find the exact sites of multiphoton imaging, we note that the histology images of the adipose–tumour boundary areas (Fig. 1, left), precancerous stroma-dominant areas (Fig. 1, right; Fig. 2, middle; Fig. 3, right), adipose–stroma boundary areas (Fig. 2, left), stroma-only areas (Fig. 2, second left), tumour-only areas (Fig. 2, second right) and tumour–stroma boundary areas (Fig. 2, right; Fig. 3, left) were typical for these representative sites.

References

36. Liu, Y. *et al.* Suppressing short-term polarization noise and related spectral decoherence in all-normal dispersion fiber supercontinuum generation. *J. Lightw. Technol.* **33,** 1814–1820 (2015).
37. Lozovoy, V. V., Pastirk, I. & Dantus, M. Multiphoton intrapulse interference. IV. Ultrashort laser pulse spectral phase characterization and compensation. *Opt. Lett.* **29,** 775–777 (2004).
38. Liu, Y., Tu, H., Benalcazar, W. A., Chaney, E. J. & Boppart, S. A. Multimodal nonlinear imaging by pulse shaping of a fiber supercontinuum from 900 to 1160 nm. *IEEE J. Sel. Top. Quantum Electron.* **18,** 1209–1214 (2012).
39. Pegoraro, A. F. *et al.* Optimally chirped multimodal CARS microscopy based on a single Ti:sapphire oscillator. *Opt. Express* **17,** 2984–2996 (2009).
40. Arafah, B. M., Finegan, H. M., Roe, J., Manni, A. & Pearson, O. H. Hormone dependency in *N*-nitrosomethylurea-induced rat mammary tumors. *Endocrinology* **111,** 584–588 (1982).
41. Crist, K. A., Chaudhuri, B., Shivaram, S. & Chaudhuri, P. K. Ductal carcinoma *in situ* in rat mammary gland. *J. Surg. Res.* **52,** 205–208 (1992).
42. Singh, M., McGinley, J. N. & Thompson, H. J. A comparison of the histopathology of premalignant and malignant mammary gland lesions induced in sexually immature rats with those occurring in the human. *Lab. Invest.* **80,** 221–231 (2000).

© 2016 Macmillan Publishers Limited. All rights reserved